

TIFR Near Infrared Imaging Camera-II on the 3.6-m Devasthal Optical Telescope

T. Baug^{1,2}, D.K. Ojha², S.K. Ghosh^{2,3}, S. Sharma¹, A.K. Pandey¹, Brijesh Kumar¹, Arpan Ghosh¹, J.P. Ninan^{2,4}, M.B. Naik², S.L.A. D'Costa², S.S. Poojary², P.R. Sandimani², H. Shah², B. Krishna Reddy¹, S.B. Pandey¹, and H. Chand¹

¹*Aryabhata Research Institute of Observational Sciences, Manora Peak, Nainital 263 001, India; tapas.polo@gmail.com*

²*Tata Institute of Fundamental Research, Homi Bhabha Road, Colaba, Mumbai 400 005, India*

³*National Centre for Radio Astrophysics, Tata Institute of Fundamental Research, Pune 411 007, India*

⁴*Department of Astronomy and Astrophysics, The Pennsylvania State University, University Park, USA*

Received (to be inserted by publisher); Revised (to be inserted by publisher); Accepted (to be inserted by publisher);

TIFR Near Infrared Imaging Camera-II is a closed-cycle Helium cryo-cooled imaging camera equipped with a Raytheon 512×512 pixels InSb Aladdin III Quadrant focal plane array having sensitivity to photons in the 1–5 μm wavelength band. In this paper, we present the performance of the camera on the newly installed 3.6-m Devasthal Optical Telescope (DOT) based on the calibration observations carried out during 2017 May 11–14 and 2017 October 7–31. After the preliminary characterization, the camera has been released to the Indian and Belgian astronomical community for science observations since 2017 May. The camera offers a field-of-view of $\sim 86''.5 \times 86''.5$ on the DOT with a pixel scale of $0''.169$. The *seeing* at the telescope site in the near-infrared bands is typically sub-arcsecond with the best *seeing* of $\sim 0''.45$ realized in the near-infrared *K*-band on 2017 October 16. The camera is found to be capable of deep observations in the *J*, *H* and *K* bands comparable to other 4-m class telescopes available world-wide. Another highlight of this camera is the observational capability for sources up to Wide-field Infrared Survey Explorer (WISE) W1-band (3.4 μm) magnitudes of 9.2 in the narrow *L*-band (*nbL*; $\lambda_{\text{cen}} \sim 3.59 \mu\text{m}$). Hence, the camera could be a good complementary instrument to observe the bright *nbL*-band sources that are saturated in the *Spitzer*-Infrared Array Camera ($[3.6] \lesssim 7.92$ mag) and the WISE W1-band ($[3.4] \lesssim 8.1$ mag). Sources with strong polycyclic aromatic hydrocarbon (PAH) emission at 3.3 μm are also detected. Details of the observations and estimated parameters are presented in this paper.

Keywords: instrumentation: detectors, instrumentation: photometers, methods: observational

1. Introduction

The Infrared Astronomy group of Tata Institute of Fundamental Research (TIFR), Mumbai, India is continuously involved in developing ground-based and space-based near- and far-infrared photometers/imagers and spectrographs. The TIFR near infrared imaging camera-I (TIRCAM1) having a 58×62 pixels InSb focal plane array (FPA), was the first array camera developed by the group. Using the TIRCAM1, observations were mainly carried out during the period 2001–2006 at the focal plane of the 1.2-m Mount Abu infrared telescope (f/13 Cassegrain focus) of Physical Research Laboratory, India. More details about this camera and the related works can be found elsewhere in Ghosh & Naik (1993), Ghosh (2005) and Ojha et al. (2002, 2003, 2006).

Later in 2012, the camera was upgraded with a larger Raytheon 512×512 pixels InSb Aladdin III Quadrant FPA. The optics was re-designed for use of the camera at the focal plane of the 2-m Himalayan *Chandra* Telescope (HCT; f/9) operated by Indian Institute of Astrophysics, India^a, and the 2-m Girawali Telescope (f/10) operated by Inter-University Centre for Astronomy and Astrophysics, India^b. The camera was therefore renamed as TIFR Near Infrared Imaging Camera-II (TIRCAM2). The detector is cooled to an operating temperature of 35 K by a closed-cycle Helium cryo-cooler. The InSb array in the TIRCAM2

¹Corresponding author.

^ahttps://www.iap.res.in/iao_telescope

^b<http://igo.iucaa.in/>

is sensitive to photons in the 1–5 μm wavelength band. However, the optics in the TIRCAM2 restricts the operating wavelength range below $\sim 3.8 \mu\text{m}$. The camera accommodates seven selectable standard near-infrared (NIR) filters (see Table 1) for imaging observations.

The TIRCAM2 has been recently mounted at the axial port (shown in Figure 1) of the 3.6-m Devasthal Optical Telescope (DOT; latitude: $29^\circ.1971$ N, longitude: $79^\circ.6841$ E, altitude: 2450 m). The field-of-view (FoV) of the camera on the DOT is $86''.5 \times 86''.5$, with a pixel scale of $0''.169 \pm 0''.002$. In typical $1''$ *seeing* conditions, the TIRCAM2 therefore heavily samples the stellar profile. Such a pixel sampling is ideal for high accuracy photometry, particularly of bright NIR sources. The dark current measured was $\sim 12 \text{ e}^- \text{ sec}^{-1}$, and the readout noise was $\sim 30 \text{ e}^-$ (single readout) for the FPA. This value of dark current is comparatively higher, possibly because of a thermal leak. The median gain of the detector was found to be $\sim 10 \text{ e}^- \text{ ADU}^{-1}$. Elaborative technical details of the TIRCAM2 can be found in Naik et al. (2012). One of the filters (narrow H_2 -band filter; $\lambda_{\text{cen}} \sim 2.12 \mu\text{m}$, $\Delta\lambda \sim 0.03 \mu\text{m}$) in the camera, has been replaced by the standard broad H -band ($\lambda_{\text{cen}} \sim 1.60 \mu\text{m}$, $\Delta\lambda \sim 0.30 \mu\text{m}$) filter (see Table 1) before commissioning it on the DOT. The TIRCAM2 also accommodates the Bracket-gamma filter ($\lambda_{\text{cen}} \sim 2.16 \mu\text{m}$, $\Delta\lambda \sim 0.03 \mu\text{m}$). This particular filter is extremely useful in the study of emission line sources, and star-forming regions.

In this article, we report on the calibration and performance of the TIRCAM2 at the focal plane of the 3.6-m DOT, the largest optical aperture in the country till date. The calibration observations presented in this paper were mainly carried out in two successive cycles, before and after the monsoon in the year 2017 (i.e., Cycles 2017A and 2017B). The paper is arranged in the following manner. The details of the observations and the data reduction are presented in Section 2. The performance of the TIRCAM2, estimation of several observational parameters, and characterization of the camera on the DOT are presented in Section 3. Finally, a summary of the performance of the TIRCAM2 is presented in Section 4.

2. Observations and Data reduction

The TIRCAM2 was shipped to Devasthal for installation and commissioning with the 3.6-m DOT in 2016 May. The camera was installed on the telescope on 2016 June 1. On the following night, 2016 June 2, first light was obtained with the TIRCAM2 instrument on the DOT. The observations during 2016 June could not be carried out due to the monsoons and cloudy weather. Preliminary observations using the TIRCAM2 with the 3.6-m DOT were performed only during 2017 January 9–16. However, we were unable to obtain systematic data required for calibration, during that run again due to interruption by the clouds. Primary part of the calibration observations presented in this paper were carried out during the early science run of the DOT (i.e., 2017A) from 2017 May 11–22. During this period the sky was clear with excellent sub-arcsec *seeing* conditions ($\sim 0''.6$ – $0''.9$) in the K -band, and that is why we could obtain fruitful observations in spite of highly humid pre-monsoon weather condition (relative humidity typically $>70\%$) at the Devasthal site. Few more additional calibration observations were also performed during 2017 October 7–31, the second phase of the early science run (cycle 2017B) after the monsoon. The *seeing* during this run was generally $\lesssim 1''$. However, the best *seeing* of $0''.45$ was noted on 2017 October 16.

The standard NIR observation strategy was followed while observing with the TIRCAM2 which involves acquisition of dark frames, along with the observations of flat frames during the morning and evening twilights. In general, short exposure observations of the target object in at least 3 dithered positions were deemed sufficient. Typically, in the JH bands, multiple frames of 50 s exposure were acquired, while in the K -band several 10 s frames were acquired to avoid saturation. Due to large background in the nbL -band, several hundreds to thousands of frames were acquired with a short exposure of 50 ms for each frame. Observations of nearby standard stars, immediately before or after the observations of science targets, were also done for flux calibration. Additionally, we observed blank sky frames of identical exposures as of the target star. This is to remove a non-uniform additive illumination in TIRCAM2 images. Master sky frame was generated by median combining all the observed sky frames. It is however possible to construct sky frames by median combining the science target frames if the observed field is not too crowded. During data reduction, sky background was removed from the science frame by subtracting the master-sky images after flat-fielding. We have also constructed a TIRCAM2 bad pixel mask (discussed in Section 3.2) which

was applied to all the science images before performing the photometric reduction.

Photometric reduction was carried out using IRAF^c software, following the standard procedures. All the raw scientific frames were first dark subtracted, and then corrected by a master flat. The point sources in those frames were identified using the DAOFIND package of IRAF (Stetson, 1992). Aperture photometry was carried out on the frames with isolated sources. For the crowded frames, point-spread-function (PSF) photometry was performed. The average PSF was defined by choosing at least 9 isolated stars in the frame. Subsequently, the PSF photometry was performed on the identified point sources in that frame using the average PSF. The instrumental magnitudes were finally calibrated to the standard system using the Two Micron All Sky Survey (2MASS) magnitudes (Cutri et al., 2003) of a few non-variable stars in the frame.

3. Performance of the TIRCAM2 on the DOT

In this section, we present the performance of the TIRCAM2 on the DOT and the estimation of several parameters based on the calibration observations.

3.1. Seeing at Devasthal

The FWHM *seeing* during the calibration nights was typically sub-arcsecond in all JHK bands. The best *seeing* obtained during the cycle 2017A was about 0''.6 on 2017 May 22 (see a *K*-band stellar image in the top-left panel of Figure 2). We have also shown the radial profile of the stellar image in the top-right panel of Figure 2. The full width at half maxima (FWHM) of the stellar profile is 3.5 pixels which converts to $\sim 0''.6$ on the sky. However, during cycle 2017B, a *seeing* of 0''.45 (~ 2.65 pixels) was obtained in the *K*-band on 2017 October 16, and the corresponding stellar image and the radial profile are also shown in the lower panels of Figure 2, respectively. Hence, it seems that under normal sky conditions, the typical *seeing* at the DOT site should be sub-arcsecond in the NIR bands. Such a sub-arcsecond *seeing* is extremely useful not only to resolve sources in crowded regions but also to perform accurate photometry. It is also worth mentioning here, that the pixel scale of the TIRCAM2 ($\sim 0''.169$) is optimal for sub-arcsecond *seeing* conditions at Devasthal. It must be mentioned here that the variation of the PSF over the FoV is negligible compared to the *seeing* limitation.

3.2. Bad pixel mask

Every detector array has a certain percentage of bad, hot and cold pixels. Bad pixels are considered to be those which show substantially high variations with respect to the median counts in the resultant frame obtained by dividing two flat frames observed in the high and the low incident flux. For the TIRCAM2, we found that pixels having variations more than 8σ are generally bad. Similarly, the hot and cold pixels are those pixels that have counts more than 8σ above and below the median value, respectively, in a dark readout frame. It is noted that not all hot and cold pixels are really bad pixels that need to be masked. Efficiency of many of these hot and cold pixels can be corrected by dark subtraction and flat field correction.

A bad pixel mask has been constructed for the TIRCAM2 array in order to replace the counts in bad pixels by the average counts of their neighboring pixels. The bad pixel mask of the array is shown in Figure 3.

3.3. Sky brightness

The night sky in the NIR bands is generally a few hundred times brighter than it is in the optical bands. Sky brightness in NIR bands depends on various parameters like humidity, presence of the moon and its phase, and ambient temperature. The sky brightness values were estimated from the observed science frames after subtraction of dark frames and performing flat-field correction^d. Sky brightness in the *H*, *K* and narrow *L* bands (*nbL*) was found to vary night to night. Such a variation is also expected since the

^cImage Reduction and Analysis Facility (Website: <http://iraf.net/>)

^dFor detail formula: <http://www.inquinamentoluminoso.it/cinzano/en/sbeam2.html>

water vapor contents in the atmosphere were sufficiently high and variable during the calibration nights at the DOT. In good sky conditions, we obtained sky surface brightness values (in mag arcsec⁻²) of 16.4, 14.0, 12.2 and 3.0 in *J*, *H*, *K* and *nbL* bands, respectively. The estimated sky brightness values in both the DOT cycles are consistent. Although the sky in the *K*-band at Devasthal seems to be little brighter, but overall these values are comparable with other good sites like Hanle (Ninan et al., 2014), Calar Alto and several other observatories (see Sánchez et al., 2008). The sky brightness in the *nbL*-band also seems to be comparable to the sites like Paranal^e.

3.4. Photometric sensitivity and capability

The estimation of the limiting magnitudes in the NIR bands depends on several factors like sky brightness, and reflectivity of the primary mirror (i.e., M1). We have observed several clusters to estimate the limiting magnitudes in the NIR *JHK* bands. All these clusters were observed in one dithered position in *JHK* bands. In addition, nearby sky frames were also observed with same exposure times as the target frames. Here, we report the limiting magnitudes estimated from the globular cluster M92. In both *J* and *H* bands, a total of eleven frames were acquired with each frame having an exposure time of 50 s. However, due to large background in the *K*-band, a total of hundred frames were observed with each of them having a shorter exposure time of 10 s. Accordingly, the effective exposure times in *J*, *H* and *K* bands are 550 s, 550 s and 1000 s, respectively. A three-color composite image (red: *K*-band, green: *H*-band, blue: *J*-band) of the globular cluster M92 is presented in Figure 4. In addition, a similar three-color composite RGB image of the M92, constructed using the 2MASS *JHK* bands, is also presented in Figure 4 for comparison. It can be clearly seen in the figure that the TIRCAM2 image is much deeper and has a better spatial resolution (FWHM \sim 0".8) compared to the 2MASS images (spatial resolution \sim 2"; see Skrutskie et al., 2006).

The *JHK* band magnitudes of the globular cluster M92 are used to estimate sensitivity limits. As can be seen in Figure 5, the 10σ limiting magnitudes in *JHK* bands are of 19.0, 18.8 and 18.0 mag, respectively. These numbers are comparable with the limiting magnitudes of other NIR cameras attached to several 4-m class telescopes available world-wide, e.g., Wide Field Camera attached to the 3.8-m United Kingdom Infrared Telescope (Lawrence et al., 2007) and Wide-field Infrared Camera with the 3.6-m Canada-France-Hawaii Telescope (Delorme et al., 2010).

The FoV of TIRCAM2 is comparatively small ($86''.5 \times 86''.5$). Thus, in order to examine the dithering capability and the linearity of the array, we observed two interacting galaxies, NGC 4567 and NGC 4568, in four dithered positions on 2017 May 15. The effective exposure time in each dithered position is 550 s. A mosaic of four dithered TIRCAM2 *J*-band images for a FoV ($\sim 2'.5 \times 2'.5$) covering both the interacting galaxies together is shown in Figure 6.

3.5. Exposure time calculator

It is important to estimate the required exposure time for any object before starting observations, as it eventually helps to plan and optimize the observations to be made. Hence, we have developed an *Exposure time calculator* for TIRCAM2, and also made it available online^f. It requires the name of the filter in which observations will be made, magnitude of the target source, expected signal-to-noise ratio (S/N) of the observed frame, and the desired number of frames as inputs, in order to obtain an estimate of the required exposure time for each frame. It must be noted that per frame exposure times larger than 50 s, 50 s and 10 s in *J*, *H* and *K* bands, respectively, may saturate the observed frames. In such a situation, the required exposure time has to be re-estimated by increasing the number of frames. Figure 7 shows graphs of required exposure times in the *J*, *H* and *K* bands for a magnitude range from 8–20 mag for a typical 75% reflectivity of the primary mirror, M1. Estimates of required exposure times for three different reflectivities of the M1 (i.e., 75%, 50% and 25%) are also shown in Figure 7 separately for all the three bands.

^e<https://www.eso.org/gen-fac/pubs/astclim/paranal/skybackground/>

^f<http://tirspect.pythonanywhere.com/tircam2/tircam2/>

3.6. Sub-array acquisition mode of TIRCAM2

In the full frame mode, the TIRCAM2 captures 512×512 pixels image, and the shortest possible sampling time in the full-frame mode is 256 ms. However, in the window or sub-array mode, the TIRCAM2 is able to acquire images for small box sizes ranging from 16×16 to 256×256 pixels with finer sampling times. This sub-array capability of the TIRCAM2 could therefore be useful to observe bright sources with a small exposure time in order to avoid saturation. This capability can also be employed for speckle observations generally performed to identify binary stars. Such rapid acquisition can also be useful to record light curves of fast events that occur within few hundreds of milli-seconds (e.g., lunar occultations). Twelve consecutive sky-subtracted frames of 64×64 pixels window (out of 1000 observed frames) are shown in Figure 8. The frame acquisition time for 64×64 pixels window is ~ 11 ms and the window sampling time is ~ 8.2 ms. The frame acquisition time is generally more due to the additional time needed to skip rows that fall outside the window.

3.7. Detection of sources in the *nbL*-band

Ground-based observations in the NIR *nbL*-band ($\lambda_{cen} \sim 3.59 \mu m$, $\Delta\lambda \ 0.07 \mu m$) is extremely difficult because of poor atmospheric transmission in this wavelength band. Also, this band is highly affected by the water vapor content in the Earth's atmosphere. Observations in this band have primarily been possible with satellite-based cameras, such as the *Spitzer*-Infrared Array Camera (IRAC; Reach et al., 2005), and the Wide-field Infrared Survey Explorer (WISE; Wright et al., 2010). We have performed *nbL*-band observations of several sources using the TIRCAM2 attached to the DOT. The observed *nbL*-band frames (100×100 pixels cut-outs) of sources having WISE W1-band ($3.4 \mu m$) magnitudes ranging from 3.1 to 9.2 is shown in Figure 9. The brighter sources ($W1 \leq 5.0$ mag) were observed on the calibration nights during the DOT Cycle 2017A with an effective integration time of 15 s. However, the remaining sources were observed during the DOT cycle 2017B with an effective exposure time of 125 s. It is found that sources up to 9.2 mag can be detected in the *nbL*-band of the TIRCAM2 even with an effective exposure time of about 25 s.

The sources up to W1-band magnitude of ~ 6.0 are sparsely visible even in short exposure frames of 50 ms, and thus, it allows us to align and combine those dithered frames to construct the final frame. This eventually helps us to achieve a better S/N in the combined frame. However, frames with sources fainter than W1-band magnitude of 6.0 are combined without alignment since they were not visible in the individual frames. Note that the S/N of the observed point sources can be improved substantially by aligning the frames before combining as compared to combining blindly. For example, in Figure 10, the S/N of the source, BD+68 738 ($W1 \sim 6.0$ mag), has improved from 30 to 40 when aligned and combined. Hence, it might be possible to observe sources fainter than 9.2 mag with similar exposure in the *nbL*-band using the TIRCAM2, if another bright source is present in the frame for alignment. It is worth mentioning here that point sources brighter than 7.92 mag and 8.1 mag[§] are generally saturated in the *Spitzer*-IRAC $3.6 \mu m$ frames (Churchwell et al., 2009) and the WISE W1-band images (Wright et al., 2010), respectively. The TIRCAM2 can therefore be a complementary instrument to observe the bright sources that are saturated in the *Spitzer*-IRAC and the WISE W1 frames.

We have also examined the linearity of the TIRCAM2 array in the *nbL*-band. A total of 29 sources were observed that have W1-band magnitudes ranging from 3.1–9.2. Figure 11 shows the W1-band magnitudes versus corresponding TIRCAM2 count rates. As can be seen in the figure, the array behaves linearly in this magnitude range. Since the brighter sources in the WISE W1-band ($\lesssim 8.1$ mag) are generally saturated, the photometry of these sources is determined using an indirect method. Thus, the magnitudes of brighter sources have larger errors. However, scatter in the TIRCAM2 count rates in a few measurements are seen possibly because of the variable sky background due to high humidity. It must be noted that the source having 9.2 mag is merely a 3σ detection, and hence, a large scatter (see Figure 11) in its count is not unusual as the corresponding frame is background dominated.

[§]http://wise2.ipac.caltech.edu/docs/release/allsky/expsup/sec6_3d.html#satcat

3.8. Detection of polycyclic aromatic hydrocarbon emission

The TIRCAM2 is also equipped with a polycyclic aromatic hydrocarbon (PAH) band filter ($\lambda_{cen} \sim 3.29 \mu m$, $\Delta\lambda 0.06 \mu m$). But, in general, it is difficult to observe the diffused PAH emission using ground-based telescopes. However, encouraged by the *nbL*-band detection, we observed a few known PAH emitting sources (Ghosh & Ojha, 2002). Figure 12 shows the continuum-subtracted *PAH*-band image of the Sh 2-61 region ($F_{3.3\mu m} \sim 0.4$ Jy; estimated from Verhoeff et al., 2012) observed using the TIRCAM2 at the 3.6-m DOT with an effective integration time of 13 s. *Spitzer*-IRAC 3.6 μm image which includes PAH emission, is also shown in Figure 12 for comparison. As can be seen in the figure, the TIRCAM2 could detect the central (i.e., the strongest) part of the PAH emission of the Sh 2-61 region. Hence, it might be possible to observe strong PAH sources ($F_{3.3\mu m} \gtrsim 0.4$ Jy) using the TIRCAM2.

4. Summary

The performance of the NIR imaging camera, TIRCAM2, attached to the 3.6-m DOT is found to be consistent with the expectations. At longer wavelengths, specifically at the *nbL*-band ($\lambda_{cen} \sim 3.59 \mu m$), the results are highly encouraging. In spite of high humidity ($>70\%$) during the calibration observation runs, the *seeing* was generally sub-arcsecond, and the best *seeing* obtained was $\sim 0''.45$ in the *K*-band on 2017 October 16. Deep imaging observations show that the camera has the capability to observe sources up to 19.0 mag, 18.8 mag, and 18.0 mag with 10% photometric accuracy in *J*, *H* and *K* bands, respectively, with corresponding effective exposure times of 550 s, 550 s and 1000 s. The camera is also capable of detecting the *nbL*-band sources brighter than ~ 9.2 mag, and hence, can be useful in observing bright sources that are saturated in the *Spitzer*-IRAC 3.6 μm and the WISE W1-band images. Also, the detector response is found to be linear in the *nbL*-band up to W1-band magnitude of 9.2. Overall, it is found that the TIRCAM2 with the 3.6-m DOT is adequate for deep NIR observations that are comparable to other 4-m class telescopes available world-wide. The camera is also capable of detecting strong PAH emitting sources ($F_{3.3\mu m} \gtrsim 0.4$ Jy), like Sh 2-61. The TIRCAM2 is made available at the DOT for scientific observations since 2017 May. It is also proposed to be used on one of the side ports of the DOT as the axial port will be occupied by one of the other instruments (e.g., TANSPEC^h, ADFOSCⁱ, and CCD imager) in the near future. The corresponding mechanical design is being finalized and will be fabricated soon. Overall, it is concluded that the TIRCAM2 can be highly useful for deep NIR *JHK* bands observations and may also be useful for observations in the *nbL*-band, particularly at the Devasthal site.

Acknowledgement

We thank the anonymous referee for the constructive comments that have improved the presentation of the paper. We thank the members of the Infrared Astronomy group of Department of Astronomy & Astrophysics, TIFR, and specially Mr. Rajesh Jadhav and Mr. Shailesh Bhagat for assistance and support during the installation and observations. We also like to thank the staff at the DOT, Devasthal and ARIES, for their co-operation during the installation and characterization of TIRCAM2. We specially thank Mr. Nandish Nanjappa for his valuable contributions during the installation phase. This publication has made use of data products from the Two Micron All Sky Survey (a joint project of the University of Massachusetts and the Infrared Processing and Analysis Center/ California Institute of Technology, funded by NASA and NSF).

References

- Churchwell, E., Babler, B. L., Meade, M. R., et al. 2009, *PASP*, 121, 213
 Cutri, R. M., Skrutskie, M. F., van Dyk, S., et al. 2003, The 2MASS All-Sky Catalog of Point Sources (available at <https://www.ipac.caltech.edu/2mass>)

^hTIFR-ARIES Near Infrared Spectrometer

ⁱARIES-Devasthal Faint Object Spectrograph and Camera

- Delorme, P., Albert, L., Forveille, T., et al. 2010, A&A, 518, A39
- Ghosh, S. K. 2005, Bulletin of the Astronomical Society of India, 33, 133
- Ghosh, S. K., & Ojha, D. K. 2002, A&A, 388, 326
- Ghosh, S. K., & Naik, M. B. 1993, Bulletin of the Astronomical Society of India, 21, 485
- Lawrence, A., Warren, S. J., Almaini, O., et al. 2007, MNRAS, 379, 1599
- Naik, M. B., Ojha, D. K., Ghosh, S. K., et al. 2012, Bulletin of the Astronomical Society of India, 40, 531
- Ninan, J. P., Ojha, D. K., Ghosh, S. K., et al. 2014, Journal of Astronomical Instrumentation , 3, 1450006
- Ojha, D. K., Ghosh, S. K., Tej, A., et al. 2006, MNRAS, 368, 825
- Ojha, D. K., Ghosh, S. K., Verma, R. P., & Anandarao, B. G. 2003, Bulletin of the Astronomical Society of India, 31, 467
- Ojha, D. K., Ghosh, S. K., Verma, R. P., Chakraborti, A., & Anandarao, B. G. 2002, Bulletin of the Astronomical Society of India, 30,
- Reach, W. T., Megeath, S. T., Cohen, M., et al. 2005, PASP, 117, 978
- Sánchez, S. F., Thiele, U., Aceituno, J., et al. 2008, PASP, 120, 1244
- Skrutskie, M. F., Cutri, R. M., Stiening, R., et al. 2006, AJ, 131, 1163
- Stetson, P. B. 1992, Astronomical Data Analysis Software and Systems I, 25, 297
- Verhoeff, A. P., Waters, L. B. F. M., van den Ancker, M. E., et al. 2012, A&A, 538, A101
- Wright, E. L., Eisenhardt, P. R. M., Mainzer, A. K., et al. 2010, AJ, 140, 1868-1881

Table 1. TIRCAM2 filter characteristics.

Filter Name	λ_{cen} (μm)	$\Delta\lambda$ (μm)
<i>J</i>	1.20	0.36
<i>H</i>	1.65	0.30
<i>Br-γ</i>	2.16	0.03
<i>K-cont</i>	2.17	0.03
<i>K</i>	2.19	0.40
<i>PAH</i>	3.28	0.06
<i>nbL</i>	3.59	0.07

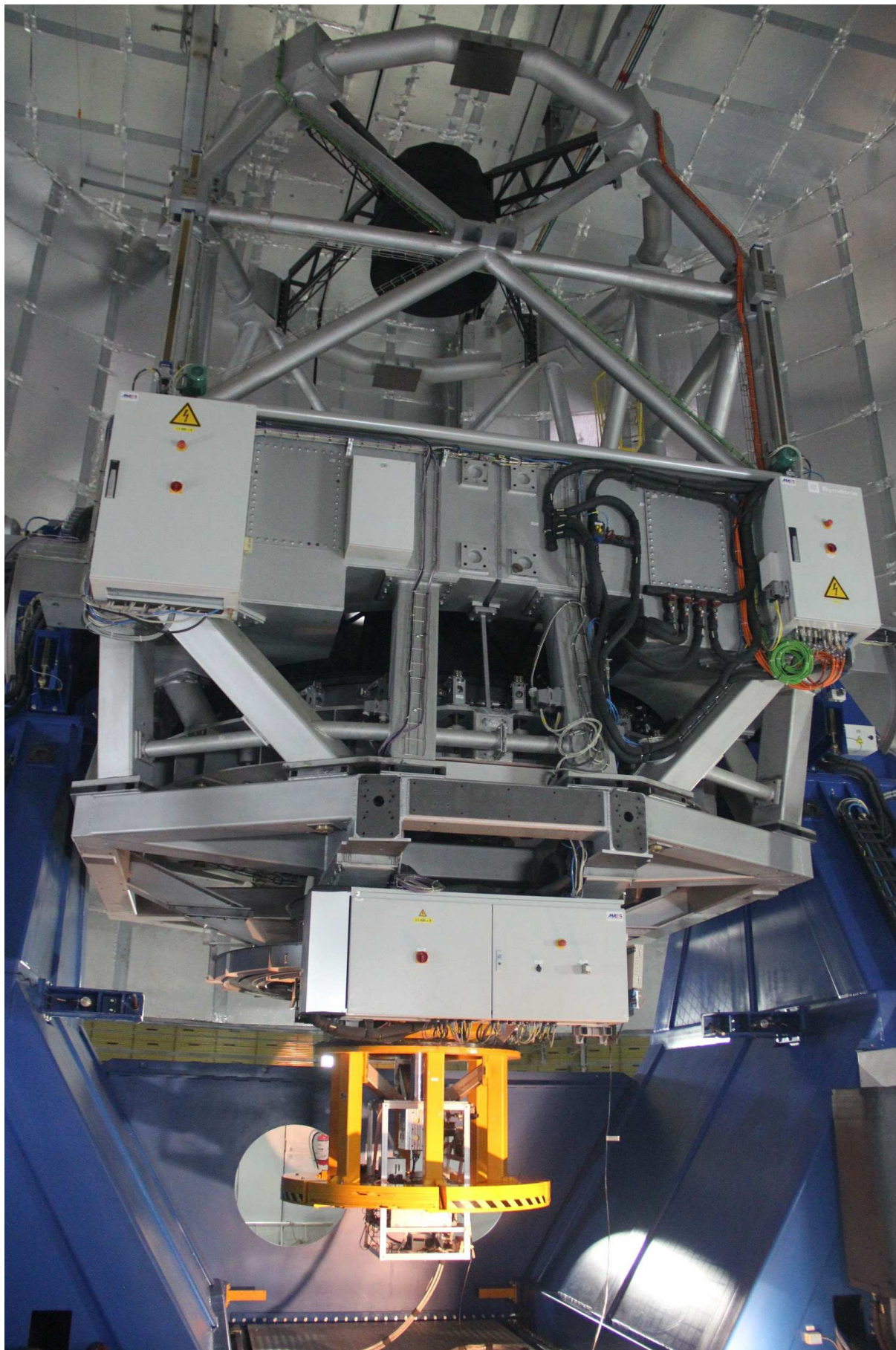


Fig. 1. The TIRCAM2 mounted at the axial port of the 3.6-m DOT.

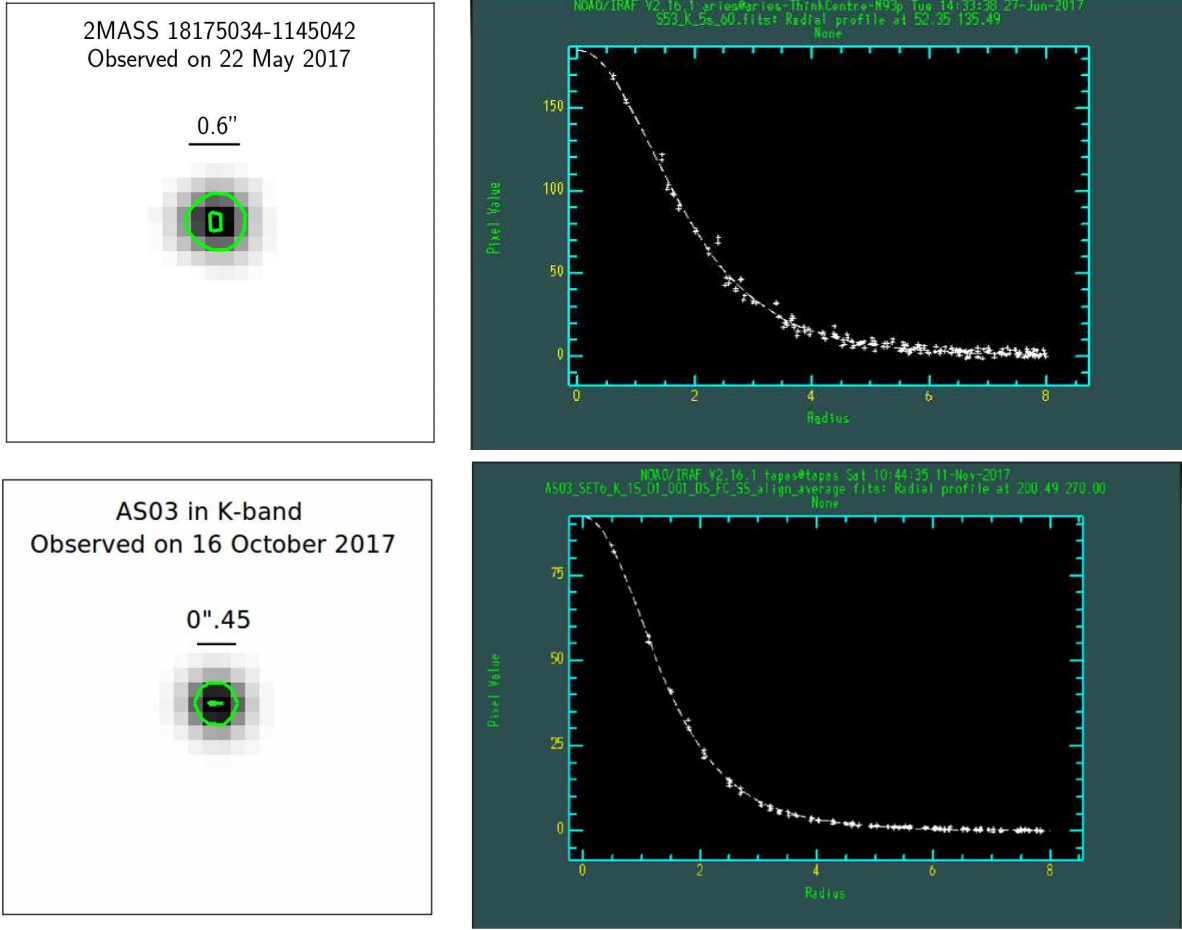


Fig. 2. *Top panels:* Cut-out of a stellar image observed with the TIRCAM2 in the *K*-band on 2017 May 22 towards the Serpens OB2 association. Typical *seeing* on this night was $\sim 0''.6$. The outer green contour shows the FWHM of the stellar image. The radial profile of the image (in pixel) is also shown in the top-right panel. *Bottom panels:* A *seeing* of $\sim 0''.45$ was observed on 2017 October 16. The stellar profile of the source AS 03 and the corresponding radial profile are shown in the left and right panels, respectively.

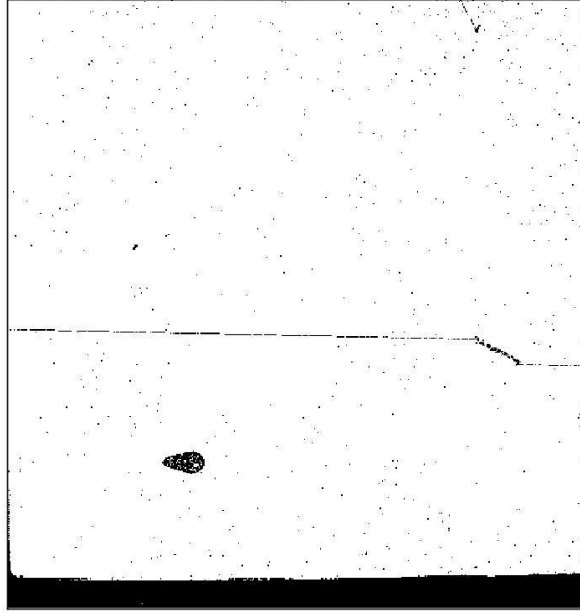


Fig. 3. Bad-pixel mask of the TIRCAM2 array. Pixels with black dots/patches represent the imperfect pixels in the TIRCAM2 array that need to be masked.

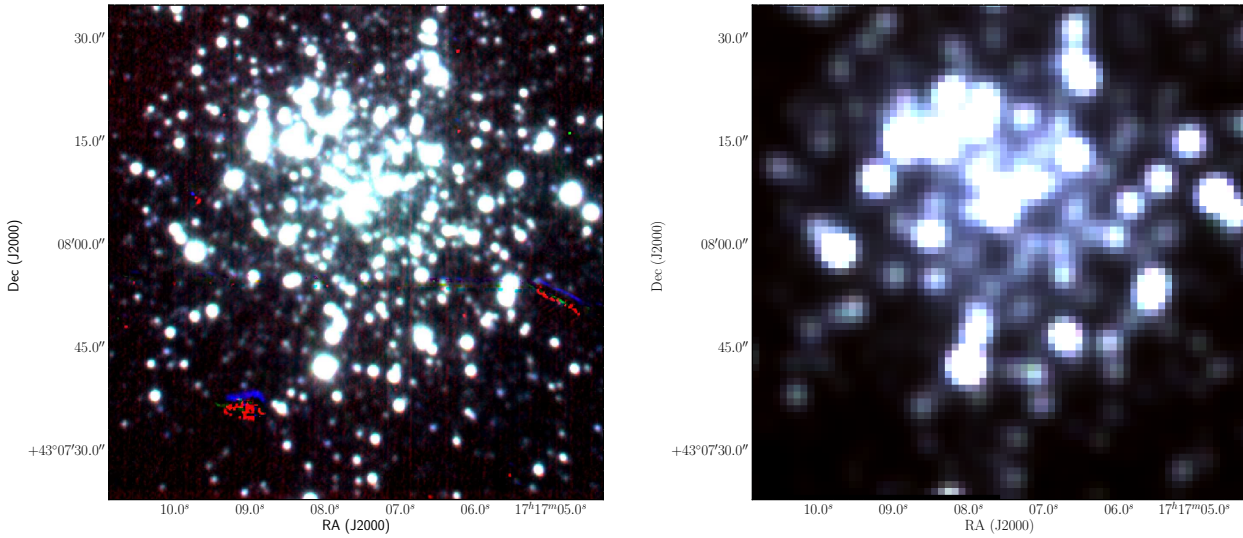


Fig. 4. The color-composite image (red: *K*-band, green: *H*-band, blue: *J*-band) of M92, a Galactic globular cluster, constructed using the frames observed with the TIRCAM2 attached to the 3.6-m DOT (left). A color-composite image for the same area generated using the 2MASS *J*, *H* and *K* band images is also shown (right) for comparison.

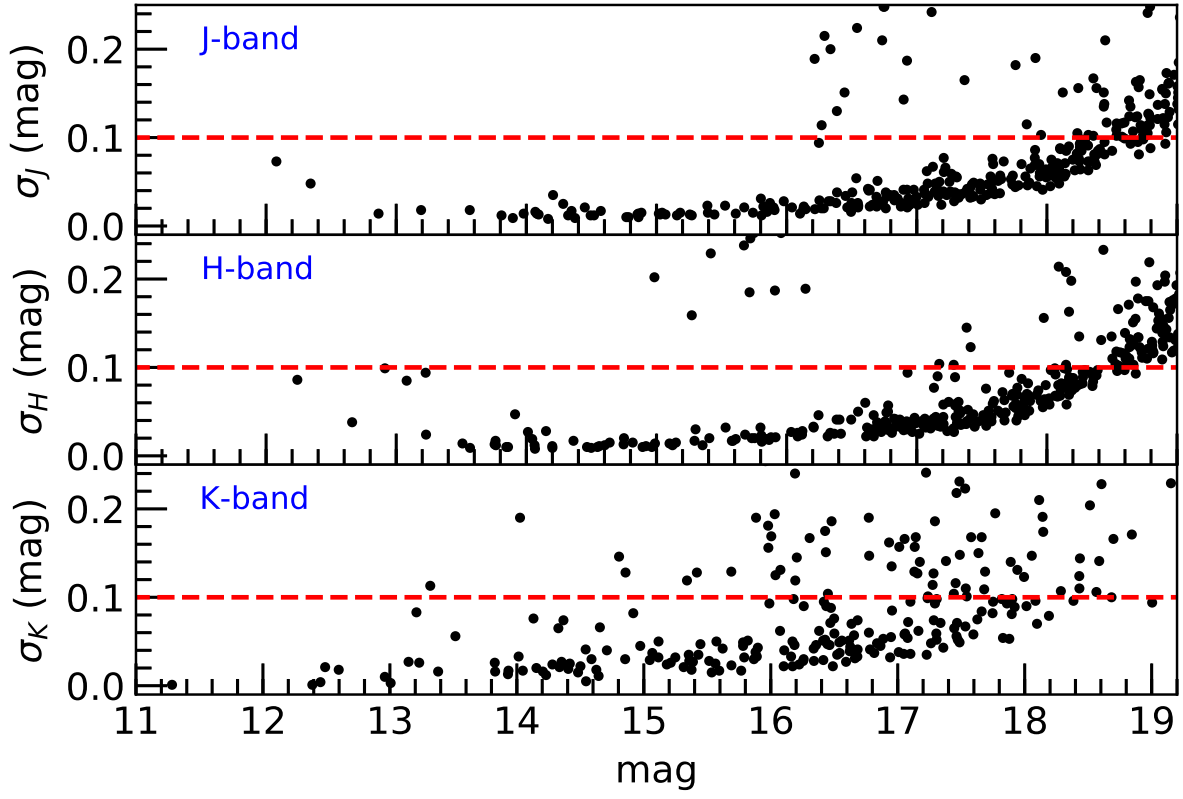


Fig. 5. J , H and K band magnitudes versus magnitude errors of the globular cluster M92 observed with effective exposure times of 550 s, 550 s and 1000s, respectively. PSF photometry was carried out for frames in all three bands with an aperture radius of one FWHM.

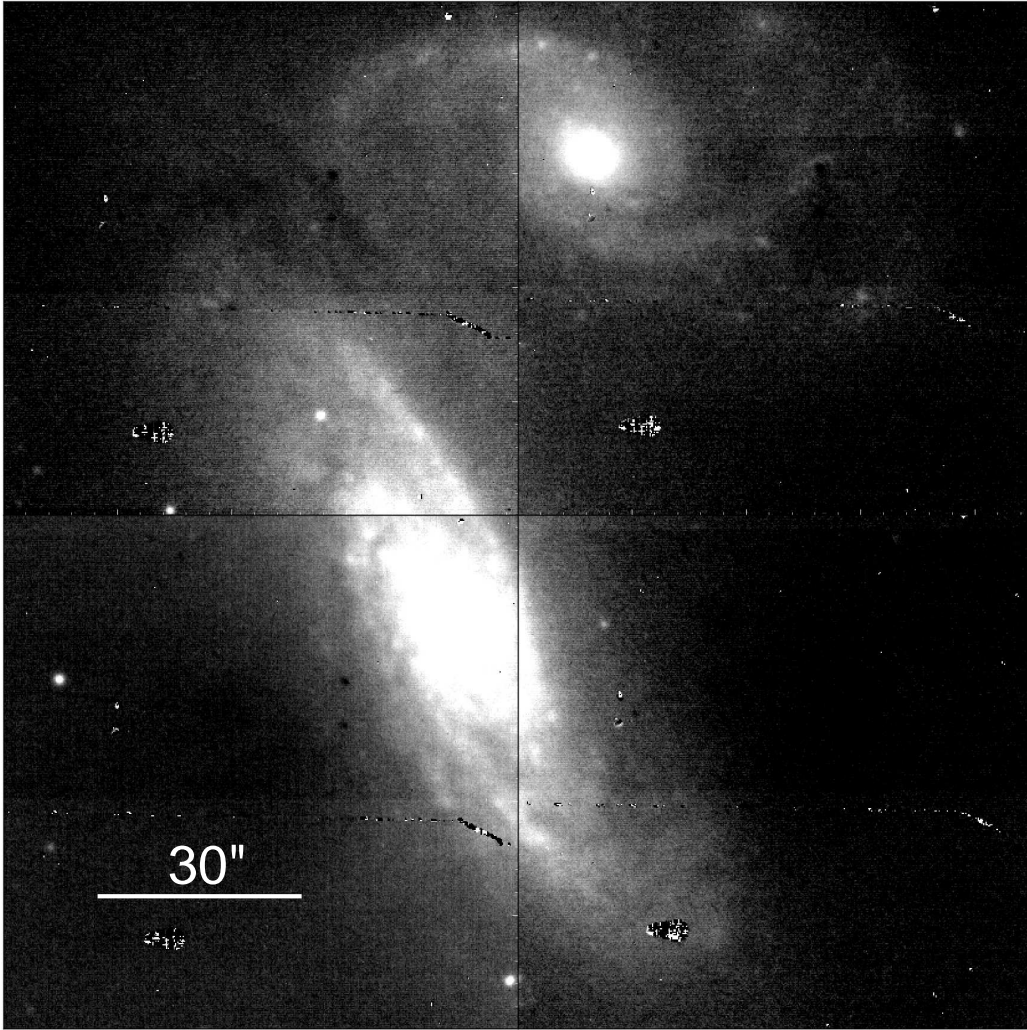


Fig. 6. Mosaic of four TIRCAM2 *J*-band images (FoV $\sim 2.5 \times 2.5$) of twin galaxies, NGC 4567 and NGC 4568, observed on 2017 May 15. North is up and East is to left.

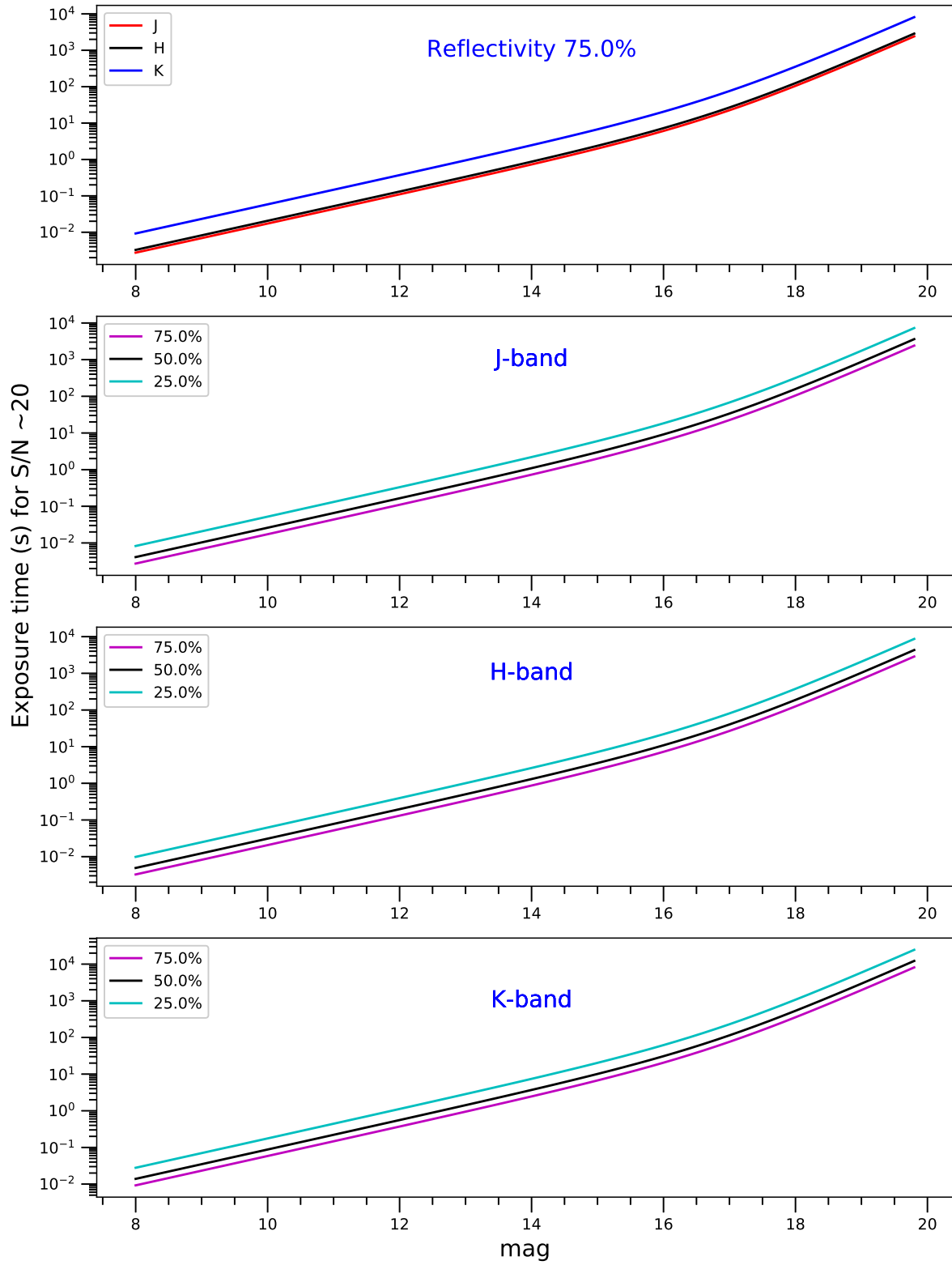


Fig. 7. Estimated exposure times required for photometry in TIRCAM2 *J*, *H* and *K* bands to achieve a $S/N \sim 20$ on a typical DOT night. The top panel shows sensitivity in all bands with 75% M1 mirror reflectivity, while other three panels show sensitivity for 75%, 50% and 25% M1 mirror reflectivities, separately for each band.

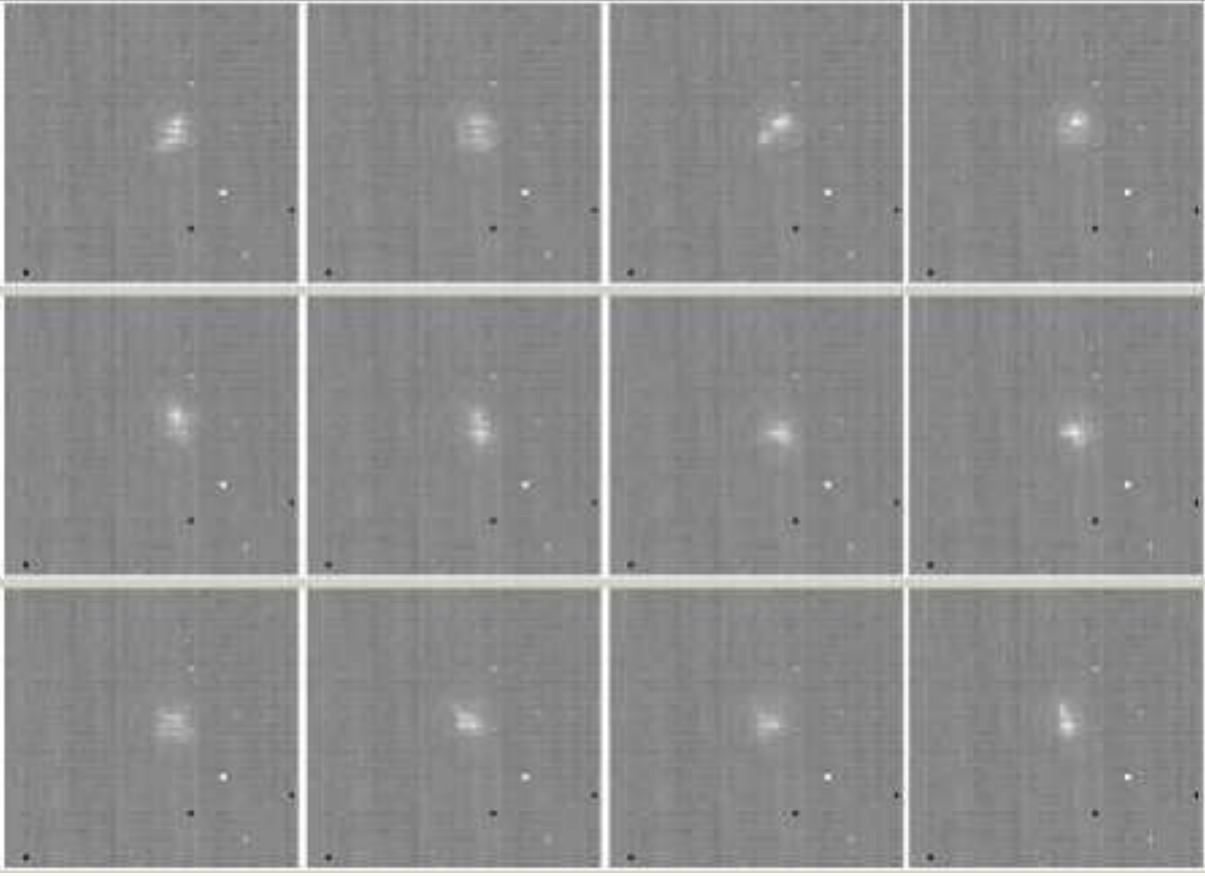


Fig. 8. Twelve consecutive sky-subtracted frames out of 1000 frames (ascending order row-wise), acquired with a window size of 64×64 pixels.

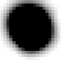
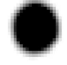






 DL Boo 3.1-mag S/N~250	 20 CVn 4.0-mag S/N~180	 HD 114253 5.0-mag S/N~102	 J215939.04+394851.0 6.5-mag S/N~78
 J220057.63+404100.4 7.0-mag S/N~50	 J015940.27+400146.9 8.0-mag S/N~17	 J225829.00+402657.5 8.7-mag S/N~8	 J015843.14+394506.1 9.2-mag S/N~3

Fig. 9. Mosaic of the *nbL*-band images (100×100 pixel cut-outs). Brighter sources ($W1 \lesssim 5.0$ mag) were observed on 2017 May 13 with effective exposure time of 15 s, and the remaining sources were observed on 2017 October 24 with effective exposure time of 125 s. Sources brighter than $W1$ -band magnitude of 6.0 were first aligned and then combined. The remaining sources were co-added blindly as these sources are not seen in the frames with exposure time of 50 ms.

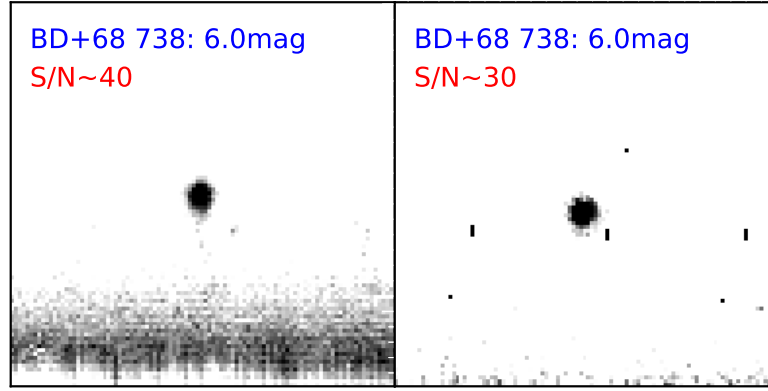


Fig. 10. The *nbL*-band frames (100×100 pixel cut-outs) of the source BD+68 738 ($W1 \sim 5.0$ mag) combined after alignment (left) and without alignment (right). Both the combined frames have an effective exposure time of 15s. The S/N improves if they are aligned and then combined.

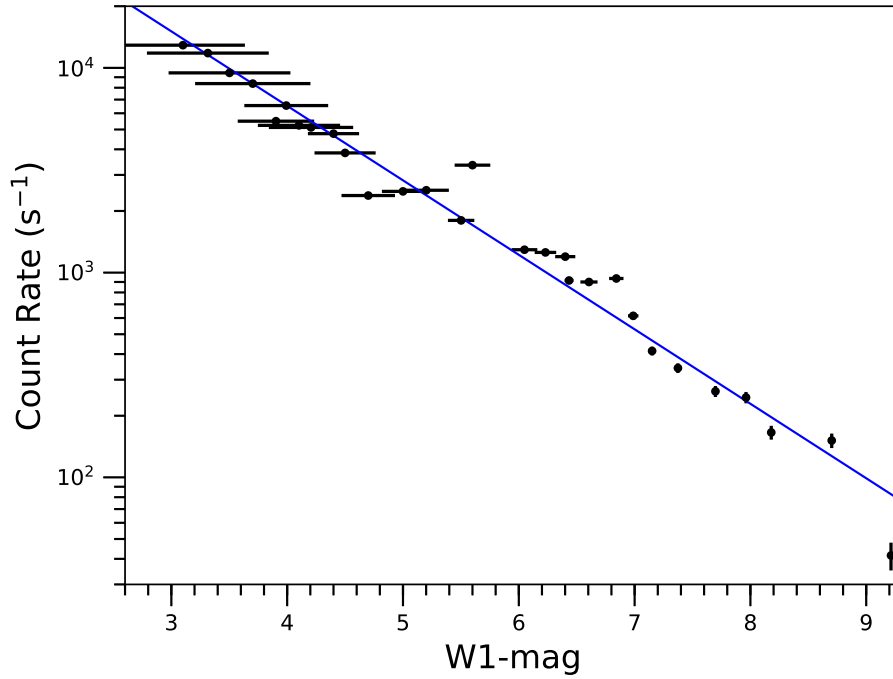


Fig. 11. The TIRCAM2 count rates *vs* the WISE W1-band magnitudes ([3.4]), showing the linear behavior of the TIRCAM2 in the *nbL*-band in the given magnitude range.

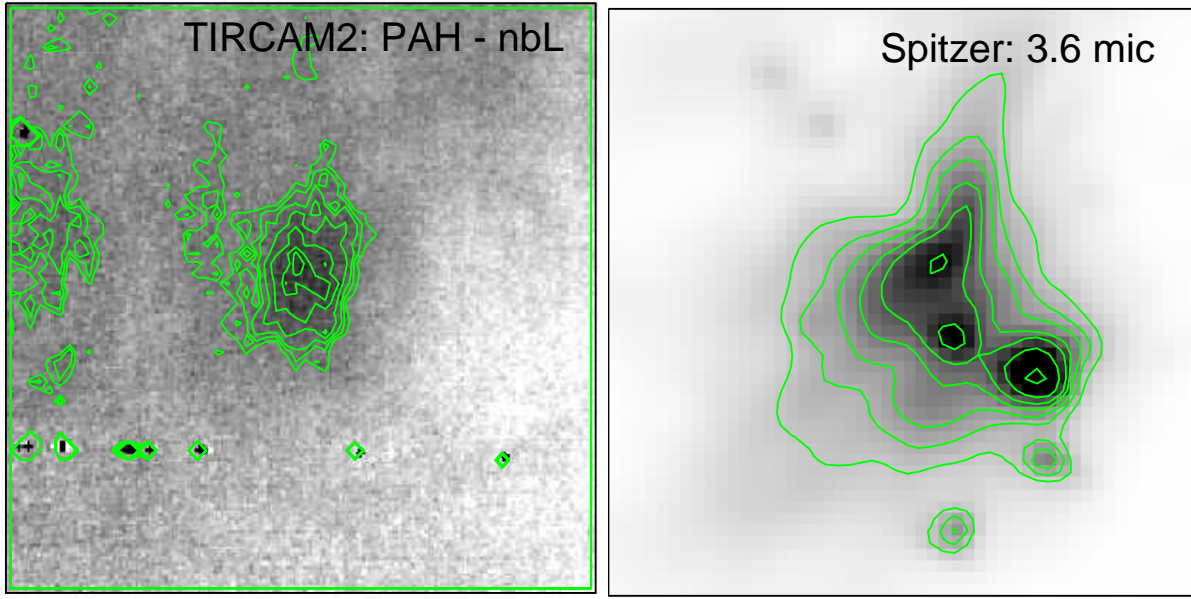


Fig. 12. The left panel shows the continuum-subtracted *PAH*-band image of $30'' \times 30''$ area around the Sh 2-61 region. Contours are overlaid for clarity. *Spitzer* $3.6 \mu m$ image for the same area is also presented for comparison (right panel).